

Towards Realistic Remote Sensing Dataset Distillation with Discriminative Prototype-guided Diffusion

Yonghao Xu, *Member, IEEE*, Pedram Ghamisi, *Senior Member, IEEE*, and Qihao Weng, *Fellow, IEEE*

Abstract—Recent years have witnessed the remarkable success of deep learning in remote sensing image interpretation, driven by the availability of large-scale benchmark datasets. However, this reliance on massive training data also brings two major challenges: (1) high storage and computational costs, and (2) the risk of data leakage, especially when sensitive categories are involved. To address these challenges, this study introduces the concept of dataset distillation into the field of remote sensing image interpretation for the first time. Specifically, we train a text-to-image diffusion model to condense a large-scale remote sensing dataset into a compact and representative distilled dataset. To improve the discriminative quality of the synthesized samples, we propose a classifier-driven guidance by injecting a classification consistency loss from a pre-trained model into the diffusion training process. Besides, considering the rich semantic complexity of remote sensing imagery, we further perform latent space clustering on training samples to select representative and diverse prototypes as visual style guidance, while using a visual language model to provide aggregated text descriptions. Experiments on three high-resolution remote sensing scene classification benchmarks show that the proposed method can distill realistic and diverse samples for downstream model training. Code and pre-trained models are available online (<https://github.com/YonghaoXu/DPD>).

Index Terms—Remote sensing, dataset distillation, text-to-image generation, image synthesis, deep learning.

I. INTRODUCTION

IN recent years, deep learning has made significant breakthroughs in remote sensing and Earth observation [1], [2], with widespread application in image interpretation tasks such as scene classification [3], object detection [4], and semantic segmentation [5]. While these achievements are certainly attributed to the increasingly powerful learning capabilities of deep neural networks [6], the emergence of large-scale, high-quality remote sensing image datasets is also indispensable [7]. However, such reliance on large-scale datasets inevitably introduces considerable storage and computational overheads

Y. Xu is with the Computer Vision Laboratory, Department of Electrical Engineering, Linköping University, 581 83 Linköping, Sweden (e-mail: yonghao.xu@liu.se).

P. Ghamisi is with Helmholtz-Zentrum Dresden-Rossendorf, Responsible AI Group, 09599 Freiberg, Germany, Lancaster University, Lancaster Environment Centre, LA1 4YR Lancaster, U.K., and also with the University of Iceland, Faculty of Electrical and Computer Engineering, Reykjavik 102, Iceland (e-mail: p.ghamisi@hzdr.de).

Q. Weng is with JC STEM Lab of Earth Observations, Department of Land Surveying and Geo-Informatics, the Research Centre for Artificial Intelligence in Geomatics, and the Research Institute for Land and Space, The Hong Kong Polytechnic University, Hung Hom, Kowloon, Hong Kong (e-mail: qihao.weng@polyu.edu.hk).

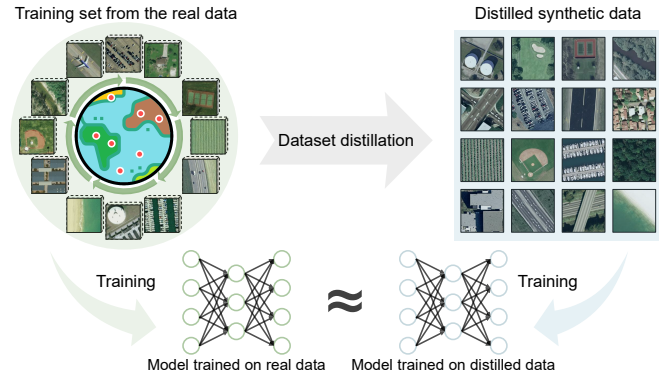


Fig. 1. Overview of the motivation for this work. Through dataset distillation, large-scale remote sensing datasets can be condensed into compact synthetic datasets that enable models to achieve performance comparable to training on the original full dataset, while reducing storage, computation, and data privacy risks.

[8]. Moreover, this dependence also raises potential risks of data leakage, especially in safety-critical Earth observation scenarios involving sensitive ground objects [9], [10]. Therefore, reducing the dependence on large-scale real datasets while maintaining model performance has become a key issue that needs to be addressed for remote sensing image interpretation.

To alleviate these challenges, dataset distillation, an emerging research direction, has recently gained increasing attention [11], [12]. As shown in Figure 1, the core idea of dataset distillation is to generate a small number of representative synthetic samples to replace the original large-scale training set to train the deep learning models, thereby reducing data storage and computing costs while maintaining model performance [13]. Unlike standard data augmentation, which aims to expand the training set to improve model robustness, dataset distillation pursues the opposite goal, i.e., to identify the “distilled essence” or a minimal set of synthetic samples required for a model to learn effectively. Although previous studies have demonstrated the effectiveness of dataset distillation in the field of natural image classification [14], [15], its direct application to remote sensing image interpretation tasks is still challenging. Compared with natural images, remote sensing images not only cover rich and complex object categories, but also exhibit diverse imaging conditions, visual styles, and semantic contexts [16], which makes it difficult to generate distilled samples that are both discriminative and

diverse. Therefore, to achieve more efficient remote sensing dataset distillation, the key is to fully exploit the rich semantic information contained in remote sensing data to accurately guide the synthesis process.

One natural idea is to use generative models to synthesize realistic remote sensing images and construct a condensed virtual training set [17]. Some studies have attempted to design generative adversarial networks (GANs) [18], auto-regressive models [17], or diffusion models [19] for remote sensing text-to-image generation. However, these methods often focus on fitting the overall visual style and texture structure of remote sensing images, making it difficult to ensure the diversity of generated data. Furthermore, existing methods usually rely on metrics such as the Inception Score [20] and Fréchet Inception Distance [21] to measure image realism, but lack specialized optimization designs for downstream interpretation tasks. As a result, even if the generated images perform well in terms of visual quality metrics, the corresponding virtual training set may not effectively improve the performance of the trained classifier [17].

Building on these observations, we propose a discriminative prototype-guided diffusion (DPD) model for remote sensing dataset distillation. Unlike existing image generation approaches that primarily focus on visual realism, our method incorporates classifier-driven guidance by injecting a cross-entropy loss from a pretrained model into the diffusion training process to enhance the discriminative quality of synthesized samples. In addition, we cluster the original training data in the latent space to identify representative and diverse prototypes as visual style guides, and leverage a vision language model (VLM) to aggregate cluster-level text descriptions into comprehensive prompts that enrich the semantic content of the generated data. Despite its simplicity, the proposed method can produce realistic and diverse samples for downstream model training. The main contributions of this paper are summarized as follows:

- 1) We systematically analyze the feasibility of dataset distillation for remote sensing data for the first time. Our results demonstrate the potential of training interpretation models with fully synthetic samples, without exposing any original data, which is particularly valuable for safety-critical remote sensing applications.
- 2) We propose a novel discriminative prototype-guided diffusion (DPD) model for remote sensing dataset distillation, which introduces classifier-driven guidance by injecting a classification consistency loss from a pre-trained model into the diffusion training process to improve the discriminative quality of the synthetic data.
- 3) We further design a dual-guidance strategy that utilizes representative visual prototypes and cluster-level text prompts to jointly enhance the diversity and semantic richness of the synthetic data.
- 4) Extensive experiments on three remote sensing scene classification datasets demonstrate that the proposed DPD can distill more realistic and diverse samples for downstream model training compared to state-of-the-art methods.

The rest of this paper is organized as follows. Section II reviews related work, Section III details the proposed DPD model, Section IV presents the datasets and experimental results, and Section V concludes the paper with some discussions.

II. RELATED WORK

A. Dataset Distillation

Dataset distillation is a recently emerging research direction that seeks to bridge the gap between massive data and limited computing resources [22]. The concept was first introduced by Wang et al., with the goal of synthesizing a compact set of samples that, although not drawn directly from the true data distribution, can train models whose performance closely approximates that of models trained on the original real dataset [13]. Early research on dataset distillation can be divided into two categories: *meta-learning-based* methods and *data matching-based* methods [11]. In the meta-learning paradigm, the distilled samples are treated as hyperparameters and optimized in a nested bi-level manner, where the inner loop trains a model on the synthetic set and the outer loop updates the synthetic data to minimize the loss on the real dataset [23], [24]. In contrast, data matching approaches update distilled samples by aligning the influence of synthetic and real data during training, usually in the form of gradients, trajectories, and feature distributions [25]–[27].

However, the synthetic data generated by these methods are not visually realistic, which has motivated recent studies to incorporate advanced generative models to enhance the realism of distilled data [15]. For example, Wang et al. utilized a generative model to store the knowledge of the target dataset, where distillation is achieved by minimizing the logit discrepancies between real and synthetic images [28]. Su et al. proposed a dataset distillation framework based on a disentangled diffusion model, which enforces consistency between real and synthetic image spaces to improve cross-architecture generalization capabilities [29]. Zhao et al. further proposed a diffusion-based framework that maps real data into a high-normality Gaussian domain to preserve structural information and generate representative latents for distilled datasets [15].

While dataset distillation has shown effectiveness in natural image classification, its direct application to remote sensing image interpretation remains challenging due to complex semantic and spatial patterns [16]. Furthermore, existing methods often ignore rich semantic cues, such as textual information, which are crucial for discriminative interpretation.

B. Text-to-Image Generation for Remote Sensing

Driven by recent advances in generative models, text-to-image generation techniques have achieved great success in the field of natural images [30] and are being increasingly explored for remote sensing applications [31]. By conditioning on natural language descriptions, such models can synthesize remote sensing images with specific semantic content, providing a new strategy for data augmentation in interpretation tasks [17].

Early work in this field focused on using GANs to synthesize remote sensing imagery. One representative example is StrucGAN, a multistage GAN that incorporates structural information from an unsupervised segmentation module to guide the generator, thereby producing structurally consistent images from text descriptions [18]. Given the limitations of GANs in terms of training stability and generative diversity, some research has explored auto-regressive models. For example, Xu et al. proposed Txt2Img-MHN, which adopts modern Hopfield networks to learn hierarchical vision prototypes from text-image embeddings in an auto-regressive manner [17]. In recent years, diffusion models have also been explored for remote sensing data generation due to their breakthrough performance in improving image quality and semantic consistency [32]. Some representative methods include Crs-diff [19], Diffusion-Sat [33], GeoRSSD [34], and Text2Earth [35].

So far, most existing work on remote sensing text-to-image generation has primarily focused on visual realism, with results usually evaluated by visual quality metrics such as IS and FID. However, since the discriminative performance of generated samples is not explicitly optimized during training, high visual quality does not always translate into improved classification performance in downstream applications [17]. Therefore, balancing the fidelity and discriminative quality of synthesized samples still remains a challenge.

C. Privacy-Preserving Learning in Remote Sensing

Given that remote sensing data may include sensitive targets in some safety-critical applications, ensuring data protection in collaborative modeling has become a critical challenge [9]. To this end, various privacy-preserving learning paradigms have been introduced in remote sensing interpretation tasks in recent years, among which federated learning and differential privacy are the most representative [36].

Federated learning enables distributed collaborative training by keeping data within each domain [37]. Participants only need to upload model parameters or gradients without sharing the original remote sensing images, which reduces the risk of data leakage to a certain extent [38]. However, federated learning also faces challenges in remote sensing tasks, such as significant data distribution heterogeneity (especially for datasets where samples are not independent and identically distributed) and high communication costs, which limit its effectiveness in large-scale applications [36]. Differential privacy, on the other hand, theoretically achieves privacy protection by injecting noise into gradients (e.g., during model training) or query results (e.g., statistics over original data), thereby preventing attackers from inferring sensitive information about specific users [39]. However, the injected noise inevitably results in a degradation of model performance [37].

Unlike the aforementioned methods, dataset distillation introduces a novel paradigm for privacy-preserving learning in remote sensing applications. Its primary objective is to replace large-scale datasets with a compact set of synthetic samples, thereby reducing computational and storage burdens while enhancing data security. In other words, while federated learning and differential privacy attempt to protect the process of

learning, dataset distillation protects the source by synthesizing a proxy dataset. This effectively decouples the model training from the raw, sensitive data.

III. METHODOLOGY

A. Problem Formulation

The objective of dataset distillation is to synthesize a compact distilled dataset $\mathcal{D} = \{(x_i, y_i)\}_{i=1}^{N_D}$ from a large-scale real dataset $\mathcal{R} = \{(x_i, y_i)\}_{i=1}^{N_R}$, where x_i denotes an image sample, y_i is its corresponding class label, and typically $N_D \ll N_R$. The distilled dataset \mathcal{D} is expected to preserve the essential knowledge of \mathcal{R} , such that models trained on \mathcal{D} can generalize to the unseen test dataset \mathcal{T} in the real domain with performance comparable to those trained on the original large-scale dataset \mathcal{R} . In practice, dataset distillation not only aims to reduce storage and computation requirements but also provides a privacy-preserving alternative by avoiding direct exposure of the original data.

B. Classification-Consistent Diffusion Training

Diffusion models are a class of probabilistic generative models that progressively transform data into noise and learn to invert this process to recover the original data distribution [40]. Formally, the forward diffusion defines a Markov chain of length T that gradually corrupts a real image sample x with Gaussian noise to obtain intermediate states:

$$x_t = \sqrt{\bar{\alpha}_t}x + \sqrt{1 - \bar{\alpha}_t}\epsilon, \quad (1)$$

where $\epsilon \sim \mathcal{N}(0, I)$ denotes a standard Gaussian noise. The term $\bar{\alpha}_t = \prod_{s=1}^t \alpha_s$ controls the noise level at timestep $t \in [1, T]$, where $\alpha_s = 1 - \beta_s$, and $\{\beta_s\}_{s=1}^T$ is a series of noise scales predefined by the diffusion process that determine the amount of Gaussian noise added at each step. Intuitively, $\sqrt{\bar{\alpha}_t}$ represents the proportion of the original image that remains after t diffusion steps, while $\sqrt{1 - \bar{\alpha}_t}$ quantifies the accumulated noise component. As t increases, $\bar{\alpha}_t$ gradually decreases towards 0, and at the final step $t = T$, the sample x_T becomes approximately pure Gaussian noise.

Inspired by the work in [41], our framework performs diffusion in a compact latent space learned by a variational autoencoder (VAE) to improve computational efficiency, as shown in Figure 2. Specifically, the VAE encoder E first maps a real image x into a latent representation $z_0 = E(x)$. The forward diffusion in Eq. (1) is then reformulated as

$$z_t = \sqrt{\bar{\alpha}_t}z_0 + \sqrt{1 - \bar{\alpha}_t}\epsilon. \quad (2)$$

During the reverse diffusion, a U-Net-based denoising network F_θ is trained to predict the noise component from the noisy latent z_t at each timestep t :

$$\epsilon_\theta = F_\theta(z_t, t, e), \quad (3)$$

where $e = E_{\text{txt}}(s)$ denotes the text embedding obtained by applying a CLIP text encoder E_{txt} to the pseudo-caption s , which provides semantic guidance during the denoising process [42]. Since the original dataset \mathcal{R} contains only image-label pairs, the pseudo-caption s is automatically generated

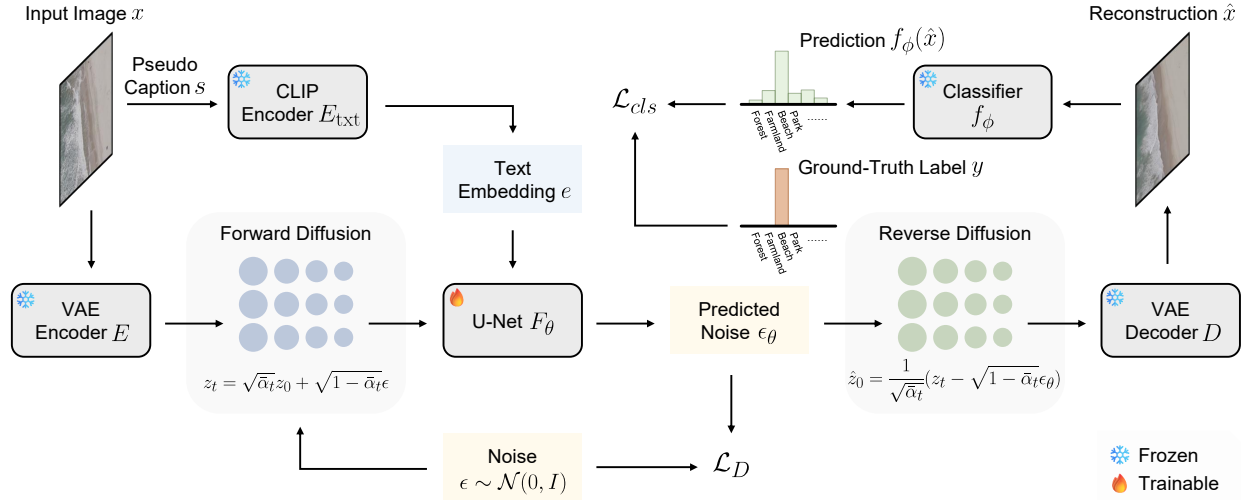


Fig. 2. Overview of the proposed classification-consistent diffusion training pipeline. Given a remote sensing image, a VAE encoder maps it into the latent space, where forward diffusion adds Gaussian noise. A U-Net then denoises the latent conditioned on CLIP text embeddings derived from the pseudo-caption, and the image is reconstructed by the VAE decoder. In addition to the diffusion loss, a pretrained classifier enforces semantic consistency through a classification loss.

Algorithm 1: Diffusion Training

Input: The training dataset $\mathcal{R} = \{(x_i, y_i)\}_{i=1}^{N_{\mathcal{R}}}$, a VAE with the encoder E and the decoder D , a CLIP text encoder E_{txt} , a VLM V , and a classifier f_{ϕ} .
Output: The trained denoising network F_{θ} .
for each iteration **do**
 Sample an image-label pair (x, y) from \mathcal{R} , a timestep $t \sim \text{Uniform}(1, T)$, and a noise $\epsilon \sim \mathcal{N}(0, I)$.
 Obtain a pseudo-caption $s = V(x)$.
 Generate the text embedding $e = E_{\text{txt}}(s)$.
 Compute the latent representation $z_0 = E(x)$.
 Generate noisy latent z_t using the forward diffusion according to Eq. (2).
 Predict noise $\hat{\epsilon}$ with F_{θ} according to Eq. (3).
 Estimate the clean latent \hat{z}_0 according to Eq. (4).
 Reconstruct image $\hat{x} = D(\hat{z}_0)$.
 Compute the diffusion loss \mathcal{L}_D and the classification consistency loss \mathcal{L}_{cls} according to Eqs. (5) and (6).
 Update θ as $\theta \leftarrow \theta - \eta \nabla_{\theta} (\mathcal{L}_D + \lambda \mathcal{L}_{cls})$.
end

using a VLM V as $s = V(x)$. The clean latent corresponding to z_t can then be estimated as

$$\hat{z}_0 = \frac{1}{\sqrt{\bar{\alpha}_t}}(z_t - \sqrt{1 - \bar{\alpha}_t}\epsilon_{\theta}). \quad (4)$$

In practice, the reverse diffusion iteratively refines the latent variable using ϵ_{θ} . At each timestep, z_t is updated toward a cleaner latent z_{t-1} according to the chosen sampling scheduler, until the final denoised latent \hat{z}_0 is obtained. During inference, this latent is decoded by the VAE decoder D to reconstruct the image as $\hat{x} = D(\hat{z}_0)$.

The diffusion model is trained by minimizing the mean squared error (MSE) between the predicted and true noise:

$$\mathcal{L}_D = \mathbb{E}_{t \sim \text{Uniform}(1, T), z_0, \epsilon, e} [\|\epsilon - F_{\theta}(z_t, t, e)\|^2]. \quad (5)$$

Note that the discriminative performance of generated samples is not explicitly optimized in the training objective of Eq. (5). Thus, high visual quality does not necessarily guarantee improved discriminative performance in downstream applications [17]. To further enhance semantic fidelity and class discriminability, we introduce a classification consistency loss \mathcal{L}_{cls} . Specifically, a pretrained classifier f_{ϕ} on the original dataset \mathcal{R} is used to predict the category of the reconstructed image \hat{x} to enforce semantic alignment between generated and real samples:

$$\mathcal{L}_{cls} = \mathbb{E}_{x, y} [-\log p_{\phi}(y|\hat{x})], \quad (6)$$

where y denotes the ground-truth label of the original remote sensing image x , and $p_{\phi}(y|\hat{x}) = f_{\phi}(\hat{x})$ represents the predicted class probability produced by f_{ϕ} . The overall training objective combines both terms as follows:

$$\mathcal{L}_{total} = \mathcal{L}_D + \lambda \mathcal{L}_{cls}, \quad (7)$$

where λ controls the weight of the classification consistency constraint.

The detailed implementation of the diffusion training process is presented in Algorithm 1.

C. Vision-Language Prototype Extraction

To effectively capture the intra-class diversity and maintain the semantic consistency of each category under limited data conditions, we propose a vision-language prototype clustering method that operates in the latent space. The goal is to identify a set of representative and semantically coherent prototypes for each category, which will serve as the foundation for subsequent dataset distillation.

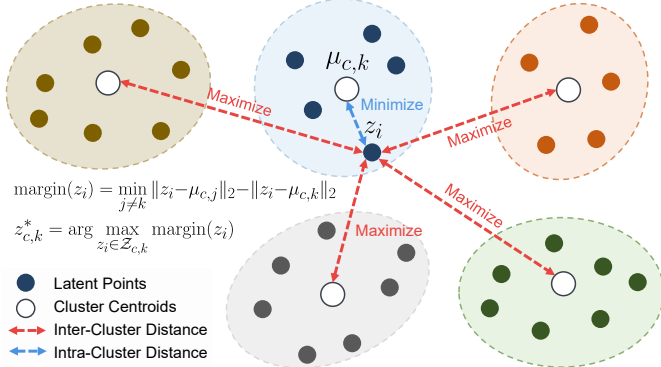


Fig. 3. Illustration of the margin-based prototype selection, where the intra-cluster distance is minimized and the inter-cluster distance is maximized to obtain the prototype $z_{c,k}^*$.

Formally, given a labeled image dataset $\mathcal{R} = \{(x_i, y_i)\}_{i=1}^{N_{\mathcal{R}}}$, each image x_i is encoded by the VAE encoder into a latent representation $z_i = E(x_i)$. For each class $c \in \{1, \dots, C\}$, we collect its latent features as $\mathcal{Z}_c = \{z_i \mid y_i = c\}$. To model the intra-class variability, we perform K-Means clustering on \mathcal{Z}_c and partition it into K sub-clusters:

$$\mathcal{Z}_{c,k} = \{z_i \mid \text{cluster}(z_i) = k\}, \quad k \in \{1, \dots, K\}. \quad (8)$$

The centroid of each cluster is computed as

$$\mu_{c,k} = \frac{1}{|\mathcal{Z}_{c,k}|} \sum_{z_i \in \mathcal{Z}_{c,k}} z_i. \quad (9)$$

Within each cluster $\mathcal{Z}_{c,k}$, we select a representative prototype sample that balances intra-cluster compactness and inter-cluster separability. Specifically, for each latent feature $z_i \in \mathcal{Z}_{c,k}$, we define a margin-based metric as

$$\text{margin}(z_i) = \min_{j \neq k} \|z_i - \mu_{c,j}\|_2 - \|z_i - \mu_{c,k}\|_2, \quad (10)$$

where the first term measures the minimum inter-cluster distance and the second term quantifies the intra-cluster compactness. $\mu_{c,j}$ refers to centroids of other clusters within the same class. The prototype for the k -th cluster is then selected as the sample that maximizes this margin:

$$z_{c,k}^* = \arg \max_{z_i \in \mathcal{Z}_{c,k}} \text{margin}(z_i). \quad (11)$$

The criterion in Eq. (11) encourages each prototype to be representative of its local cluster while remaining sufficiently distinct from other clusters, as shown in Figure 3.

After identifying visual prototypes, we enrich them with textual semantics to fully exploit the rich semantic information contained in remote sensing data to accurately guide the synthesis process. Let $\mathcal{S}_{c,k} = \{s_i\}$ denote the set of pseudo-captions associated with the samples in cluster $\mathcal{Z}_{c,k}$. Since these captions may contain redundant or inconsistent expressions, we employ a large language model (LLM) G to aggregate the multiple captions within each cluster into a unified description $s_{c,k}^* = G(\mathcal{S}_{c,k})$. Specifically, the aggregation process aims to preserve the shared semantics across captions, remove redundant or vague expressions, and highlight key visual and spatial attributes relevant to the category. As a

Algorithm 2: Dataset Distillation

Input: The training dataset $\mathcal{R} = \{(x_i, y_i)\}_{i=1}^{N_{\mathcal{R}}}$, a VAE with the encoder E and the decoder D , a CLIP text encoder E_{txt} , a VLM V , a LLM G , and a denoising network F_{θ} .

Output: The distilled dataset $\mathcal{D} = \{\hat{x}_{c,k}\}$.

for each class $c \in \{1, \dots, C\}$ **do**

- Collect latent features $\mathcal{Z}_c = \{z_i = E(x_i) \mid y_i = c\}$.
- Perform K-Means clustering on \mathcal{Z}_c to obtain $\{\mathcal{Z}_{c,k}\}_{k=1}^K$ according to Eqs. (8) and (9).
- for** each cluster $k \in \{1, \dots, K\}$ **do**

 - Select prototype latent $z_{c,k}^*$ according to Eq. (11).
 - Collect captions for the cluster as $\mathcal{S}_{c,k} = \{s_i = V(x_i) \mid z_i \in \mathcal{Z}_{c,k}\}$.
 - Aggregate $\mathcal{S}_{c,k}$ into $s_{c,k}^* = G(\mathcal{S}_{c,k})$.
 - Store prototype $(z_{c,k}^*, s_{c,k}^*)$ into \mathcal{P}_c .

- end**

end

for each class c and prototype $(z_{c,k}^*, s_{c,k}^*)$ in \mathcal{P}_c **do**

- Generate the text embedding $e_{c,k} = E_{\text{txt}}(s_{c,k}^*)$.
- Initialize latent as $z_0 \leftarrow z_{c,k}^*$.
- Estimate the clean latent $\hat{z}_{c,k}$ by reverse diffusion.
- Reconstruct the final image as $\hat{x}_{c,k} = D(\hat{z}_{c,k})$.
- Add $\hat{x}_{c,k}$ into the distilled dataset \mathcal{D} .

end

result, each class c is represented by a set of vision-language prototype pairs $\mathcal{P}_c = \{(z_{c,k}^*, s_{c,k}^*)\}_{k=1}^K$. Collectively, these multimodal prototypes provide compact yet semantically rich representations for each class, which link visual structure and textual semantics for subsequent dataset distillation.

D. Prototype-Guided Diffusion Generation

Unlike conventional diffusion models that start from random Gaussian noise [40], our approach initializes the diffusion process from a semantically meaningful visual prototype latent extracted in Section III-C. This design ensures that the generated samples preserve category semantics while exhibiting intra-class variability. Specifically, for each vision-language prototype pair $(z_{c,k}^*, s_{c,k}^*)$ of class c , we treat the visual prototype $z_{c,k}^*$ as the initial latent state of the diffusion process (i.e., initialize z_0 with $z_{c,k}^*$ in Eq. (2)). During the denoising phase, the trained diffusion model performs reverse diffusion conditioned on the prototype description $s_{c,k}^*$, yielding a denoised latent representation $\hat{z}_{c,k}$. The final distilled image is reconstructed by the VAE decoder as $\hat{x}_{c,k} = D(\hat{z}_{c,k})$.

The detailed implementation of the dataset distillation process is presented in Algorithm 2.

IV. EXPERIMENTS

A. Data Descriptions

We conduct experiments on three benchmark remote sensing scene classification datasets, including UC Merced (UCM) [44], aerial image dataset (AID) [45], and NWPU-RESISC45 [46].

TABLE I
DATASET DISTILLATION PERFORMANCE IN TERMS OF OA (%) ON THE UCM DATASET ACROSS DIFFERENT CLASSIFICATION NETWORKS.

IPC (Ratio)	Method	AlexNet	VGG16	Inception-v3	ResNet18	ResNet101	DenseNet121	DenseNet201	RegNetX-16GF
3 (6%)	Txt2Img-MHN [17]	39.01 \pm 1.74	36.97 \pm 3.30	26.90 \pm 3.08	33.98 \pm 1.77	39.16 \pm 1.68	28.69 \pm 3.39	35.45 \pm 1.92	39.92 \pm 2.11
	DiT [43]	48.72 \pm 2.75	43.86 \pm 5.10	36.54 \pm 1.78	42.34 \pm 1.47	47.83 \pm 2.32	39.96 \pm 1.83	50.17 \pm 2.01	49.68 \pm 1.84
	Minimax Diffusion [14]	44.33 \pm 1.28	39.61 \pm 3.29	34.66 \pm 1.70	41.30 \pm 2.68	44.09 \pm 3.11	35.00 \pm 2.31	42.62 \pm 3.00	47.39 \pm 2.13
	Stable Diffusion 2 [41]	39.64 \pm 2.20	43.38 \pm 4.04	51.89 \pm 1.93	52.96 \pm 2.54	59.26 \pm 1.17	52.31 \pm 2.18	58.96 \pm 1.23	61.33 \pm 1.49
5 (10%)	DPD (ours)	50.77\pm1.96	54.06\pm3.49	57.30\pm2.02	62.73\pm2.24	70.16\pm1.45	57.36\pm1.89	66.16\pm2.07	70.09\pm1.69
	Txt2Img-MHN [17]	46.30 \pm 1.44	39.12 \pm 4.64	34.74 \pm 0.92	36.84 \pm 2.43	40.17 \pm 3.34	37.12 \pm 1.61	44.23 \pm 4.17	43.90 \pm 1.97
	DiT [43]	53.70 \pm 2.88	48.10 \pm 2.74	43.36 \pm 1.88	52.91 \pm 1.33	53.62 \pm 3.05	50.17 \pm 1.77	56.38 \pm 2.68	55.86 \pm 2.00
	Minimax Diffusion [14]	49.59 \pm 2.64	47.38 \pm 3.49	42.68 \pm 2.84	45.42 \pm 1.97	47.76 \pm 3.48	44.08 \pm 2.61	50.33 \pm 2.45	51.02 \pm 1.96
10 (20%)	Stable Diffusion 2 [41]	46.50 \pm 3.31	51.09 \pm 3.90	61.59 \pm 1.33	58.33 \pm 2.93	59.44 \pm 3.61	59.73 \pm 2.15	64.40 \pm 1.84	65.25 \pm 1.20
	DPD (ours)	58.97\pm1.71	63.69\pm2.38	71.28\pm1.30	70.35\pm1.13	74.76\pm1.40	72.09\pm1.45	76.92\pm1.01	78.53\pm2.43
	Txt2Img-MHN [17]	57.07 \pm 2.52	50.55 \pm 3.33	43.31 \pm 1.22	44.38 \pm 2.39	52.65 \pm 2.27	48.48 \pm 2.55	48.82 \pm 1.38	52.72 \pm 1.75
	DiT [43]	58.38 \pm 1.94	54.23 \pm 1.91	58.23 \pm 0.81	58.22 \pm 1.50	61.71 \pm 2.98	57.78 \pm 2.76	63.55 \pm 1.44	62.55 \pm 2.86
15 (30%)	Minimax Diffusion [14]	59.13 \pm 2.62	55.01 \pm 2.96	58.24 \pm 1.54	56.50 \pm 3.03	57.10 \pm 2.21	61.16 \pm 2.66	65.47 \pm 2.34	62.60 \pm 3.20
	Stable Diffusion 2 [41]	54.26 \pm 2.21	53.10 \pm 5.14	70.19 \pm 1.47	64.83 \pm 1.35	65.39 \pm 4.05	67.90 \pm 1.63	71.38 \pm 1.49	69.70 \pm 1.86
	DPD (ours)	70.98\pm2.66	78.30\pm0.98	80.20\pm1.58	78.30\pm0.98	82.18\pm1.74	81.39\pm1.60	83.90\pm1.39	84.00\pm0.86
	Txt2Img-MHN [17]	60.46 \pm 1.74	62.08 \pm 4.95	49.60 \pm 0.43	51.58 \pm 1.72	58.65 \pm 2.59	52.82 \pm 1.84	56.51 \pm 2.82	57.73 \pm 2.18
20 (40%)	DiT [43]	61.90 \pm 2.35	59.33 \pm 4.65	63.50 \pm 1.09	64.11 \pm 1.40	64.22 \pm 2.35	64.31 \pm 1.61	70.67 \pm 1.38	68.07 \pm 2.44
	Minimax Diffusion [14]	65.73 \pm 2.12	60.29 \pm 4.58	69.61 \pm 1.18	67.08 \pm 1.58	72.01 \pm 2.30	70.19 \pm 2.04	76.70 \pm 1.51	74.37 \pm 1.61
	Stable Diffusion 2 [41]	61.36 \pm 2.24	60.81 \pm 4.07	71.74 \pm 1.36	66.81 \pm 1.74	67.08 \pm 4.09	70.35 \pm 1.52	73.68 \pm 0.84	71.79 \pm 1.75
	DPD (ours)	75.81\pm2.32	75.03\pm2.98	84.96\pm0.90	82.83\pm1.16	86.44\pm1.32	85.63\pm1.62	88.90\pm1.27	88.33\pm0.75
– (100%)	Full-data Training	92.17 \pm 1.20	91.42 \pm 2.47	95.65 \pm 0.59	95.97 \pm 0.21	95.11 \pm 1.26	97.49 \pm 0.48	97.34 \pm 0.61	97.37 \pm 0.60

Note: Best results are shown in **bold**. Here, Ratio = IPC \times $C/|\mathcal{R}|$ denotes the proportion of distilled samples to the total number of training samples, where C is the number of classes in the training set \mathcal{R} .

UCM contains 2,100 aerial scene images across 21 land-use categories, with 100 images per class. All images are RGB with a resolution of 256 \times 256 pixels (0.3 m spatial resolution) and are derived from USGS National Map aerial orthoimagery.

AID is a large-scale dataset collected from Google Earth. It is made up of 10,000 RGB images across 30 aerial scene categories. All images are annotated by remote sensing experts and provided at a fixed resolution of 600 \times 600 pixels, with spatial resolutions ranging from 0.5 m to 8 m. The number of images per class varies between 220 and 420.

NWPU-RESISC45 contains 31,500 remote sensing images across 45 scene categories, with 700 RGB images per class. It was collected by remote sensing experts from Google Earth, covering over 100 countries and regions. All images are provided at a resolution of 256 \times 256 pixels, with spatial resolutions ranging from 0.2 m to 30 m.

For UCM and AID, we randomly split each dataset into 50% for the training set \mathcal{R} and the remaining 50% for the testing set \mathcal{T} . For NWPU-RESISC45, we follow the official protocol from the original paper, where 27,000 images are used as the training set \mathcal{R} and the remaining 4,500 images serve as the testing set \mathcal{T} .

B. Experimental Settings and Evaluation

For each dataset distillation method evaluated in this study, we consider multiple images-per-class (IPC) settings, i.e., $IPC \in \{3, 5, 10, 15, 20\}$. Under each setting, the distillation model is trained on the real training set \mathcal{R} to synthesize IPC synthetic samples per class, which together form the distilled dataset \mathcal{D} .

To assess the quality of the distilled samples produced by each method, we train a classification network using the distilled dataset \mathcal{D} and report the overall accuracy (OA) on

the real test set \mathcal{T} . The evaluated network architectures include AlexNet [47], VGG16 [48], Inception-v3 [49], ResNet18 [50], ResNet101, DenseNet121 [51], DenseNet201, and RegNetX-16GF [52]. Each experiment is repeated ten times with random seeds, and we report the mean accuracy along with the standard deviation.

C. Implementation Details

Backbone models. We adopt Stable Diffusion 2 [41] as the text-to-image generative backbone for dataset distillation, which provides pretrained weights for the U-Net denoising network F_θ and the VAE encoder E and decoder D . We adopt the OpenCLIP ViT-H-14 [53] weight pretrained on LAION-2B [54] as the CLIP text encoder model E_{txt} . Note that both the VAE and CLIP models will be frozen during training. We use a ResNet-18 model pretrained on each dataset to serve as the classifier f_ϕ .

Pseudo-caption generation. For each dataset, we adopt the Qwen2.5-VL-32B model [55] to serve as the VLM V to generate pseudo-captions for all training images. The prompt used in the generation is “You are a remote sensing expert. This is a satellite image of <class name>. In one concise sentence (less than 15 words), describe the main land cover types, their spatial arrangement, colors, and notable textures or shapes. Only output the final caption.”

Training details. To enable more efficient training, the LoRA (Low-Rank Adaptation) technique [56] is adopted when fine-tuning the U-Net denoising network F_θ . The model is trained using the AdamW optimizer [57] with a learning rate of $1e-4$, batch size of 8 per GPU, and 80,000 training steps at the resolution of 512 \times 512. The weight of the classification consistency loss is set to $\lambda = 0.3$ (see Section IV-F for a detailed analysis). The classifier f_ϕ is trained on the original

TABLE II
DATASET DISTILLATION PERFORMANCE IN TERMS OF OA (%) ON THE AID DATASET ACROSS DIFFERENT CLASSIFICATION NETWORKS.

IPC (Ratio)	Method	AlexNet	VGG16	Inception-v3	ResNet18	ResNet101	DenseNet121	DenseNet201	RegNetX-16GF
3 (1.8%)	Txt2Img-MHN [17]	32.89 \pm 2.85	25.91 \pm 4.14	22.34 \pm 1.05	28.10 \pm 1.02	37.67 \pm 0.79	27.91 \pm 1.41	36.88 \pm 0.46	39.86 \pm 1.17
	DiT [43]	27.98 \pm 2.42	23.44 \pm 3.65	19.42 \pm 1.29	25.94 \pm 2.67	33.63 \pm 1.17	24.26 \pm 1.33	32.11 \pm 1.47	33.77 \pm 1.99
	Minimax Diffusion [14]	18.78 \pm 2.00	15.99 \pm 1.99	13.43 \pm 1.07	16.99 \pm 1.05	19.90 \pm 1.28	15.46 \pm 1.68	20.25 \pm 1.47	23.18 \pm 1.60
	Stable Diffusion 2 [41]	39.19 \pm 2.04	33.39 \pm 2.63	40.67 \pm 1.76	46.86 \pm 1.87	56.96 \pm 1.35	47.00 \pm 1.38	56.22 \pm 1.25	55.48 \pm 1.84
5 (3%)	DPD (ours)	46.30\pm1.87	44.76\pm2.01	45.57\pm1.78	54.21\pm0.95	64.33\pm0.94	52.52\pm1.36	63.22\pm1.06	67.10\pm0.74
	Txt2Img-MHN [17]	38.16 \pm 1.92	34.16 \pm 2.55	31.00 \pm 0.95	38.36 \pm 1.85	41.16 \pm 1.52	37.83 \pm 1.70	43.69 \pm 1.10	39.55 \pm 1.85
	DiT [43]	38.84 \pm 1.48	29.73 \pm 3.40	29.73 \pm 1.09	37.41 \pm 1.17	42.06 \pm 1.40	35.63 \pm 1.56	41.17 \pm 1.25	42.38 \pm 1.45
	Minimax Diffusion [14]	23.93 \pm 2.32	19.06 \pm 2.86	20.64 \pm 1.34	24.84 \pm 1.61	25.69 \pm 1.53	23.80 \pm 1.10	27.18 \pm 1.36	28.64 \pm 1.30
10 (6%)	Stable Diffusion 2 [41]	43.30 \pm 2.76	40.54 \pm 4.23	50.68 \pm 1.13	54.08 \pm 1.54	59.68 \pm 2.42	55.17 \pm 1.21	60.20 \pm 1.29	58.82 \pm 0.76
	DPD (ours)	51.45\pm2.84	48.39\pm4.48	57.17\pm1.40	60.73\pm1.27	69.04\pm0.82	63.70\pm0.63	69.20\pm1.21	73.52\pm1.41
	Txt2Img-MHN [17]	45.68 \pm 2.20	41.23 \pm 1.49	39.60 \pm 2.33	42.90 \pm 1.48	47.99 \pm 2.02	43.89 \pm 1.11	46.27 \pm 1.40	47.53 \pm 1.93
	DiT [43]	46.34 \pm 2.00	32.37 \pm 3.84	38.43 \pm 1.65	43.66 \pm 1.47	48.34 \pm 2.54	43.69 \pm 2.24	48.30 \pm 1.58	51.00 \pm 1.62
15 (9%)	Minimax Diffusion [14]	32.13 \pm 1.64	28.00 \pm 2.08	27.61 \pm 1.54	32.88 \pm 1.17	31.57 \pm 2.32	31.09 \pm 2.43	34.00 \pm 1.27	37.25 \pm 1.45
	Stable Diffusion 2 [41]	45.77 \pm 2.71	44.64 \pm 4.61	59.64 \pm 1.81	57.92 \pm 1.30	61.32 \pm 1.69	60.62 \pm 1.67	64.10 \pm 1.38	60.33 \pm 2.10
	DPD (ours)	60.24\pm1.88	58.06\pm4.56	69.30\pm0.97	70.86\pm1.45	75.45\pm1.45	73.93\pm0.61	77.63\pm1.01	78.38\pm1.38
	Txt2Img-MHN [17]	44.76 \pm 1.94	40.45 \pm 5.81	41.09 \pm 0.95	45.88 \pm 2.25	47.30 \pm 1.81	45.05 \pm 3.80	49.59 \pm 1.67	46.45 \pm 4.39
20 (12%)	DiT [43]	47.49 \pm 1.92	38.74 \pm 4.40	42.81 \pm 2.01	43.73 \pm 3.01	47.51 \pm 3.45	46.53 \pm 1.86	50.15 \pm 2.55	45.83 \pm 3.07
	Minimax Diffusion [14]	35.67 \pm 1.66	30.50 \pm 3.42	31.05 \pm 2.09	37.74 \pm 2.03	37.66 \pm 2.20	38.52 \pm 2.68	41.89 \pm 2.36	41.97 \pm 2.36
	Stable Diffusion 2 [41]	48.99 \pm 1.97	45.75 \pm 2.00	60.13 \pm 1.78	55.62 \pm 1.75	52.48 \pm 4.29	59.79 \pm 2.04	64.58 \pm 1.38	56.04 \pm 3.43
	DPD (ours)	64.66\pm1.44	59.59\pm4.01	71.73\pm1.15	70.08\pm1.50	73.01\pm1.36	75.80\pm1.68	77.85\pm2.09	76.07\pm2.53
– (100%)	Full-data Training	88.34 \pm 1.28	89.36 \pm 2.43	92.86 \pm 0.38	93.38 \pm 0.82	93.25 \pm 0.65	95.27 \pm 0.39	95.18 \pm 0.26	94.89 \pm 0.78

Note: Best results are shown in **bold**. Here, Ratio = IPC \times $C/|\mathcal{R}|$ denotes the proportion of distilled samples to the total number of training samples, where C is the number of classes in the training set \mathcal{R} .

training set \mathcal{R} , optimized using the Adam optimizer [58] with a learning rate of $1e-4$ and a batch size of 32 for 10 epochs. The weights of f_ϕ then get frozen during the training of the diffusion model. All experiments are conducted on a cluster with four NVIDIA A100 GPUs.

Prototype extraction. For each category in \mathcal{R} , we conduct K-Means clustering on the VAE latent space, where the number of clusters is set to $K = \text{IPC}$ under the dataset distillation setting. We adopt the Qwen3-4B model [59] to serve as the LLM G to aggregate the multiple pseudo-captions within each cluster into a unified description $s_{c,k}^* = G(\mathcal{S}_{c,k})$. The prompt used in the generation is “You are a remote sensing expert. Combine the following captions into a single concise, non-redundant, and representative description for the <class name> category. Requirements: (1) one sentence only; (2) ≤ 25 words; (3) objective and specific; (4) include key land-cover elements, layout/structure, and salient textures/patterns; (5) avoid filler phrases like ‘there is/are’ and avoid repetition.”

D. Quantitative Results

We compare the proposed DPD with four state-of-the-art methods including Txt2Img-MHN [17], DiT [43], Minimax Diffusion [14], and Stable Diffusion 2 [41]. For text-to-image generation methods such as Txt2Img-MHN and Stable Diffusion 2, we adopt a unified text template, “A satellite image of <class name>”, as the textual description for images belonging to the <class name> category. For class-conditioned image generation methods, including DiT and Minimax Diffusion, the category index is used as the conditioning signal for image synthesis. All compared methods are trained using their official GitHub implementations.

Tables I–III report the quantitative comparison results on the UCM, AID, and NWPU datasets under different IPC

settings and classification network architectures. Here, *Full-data Training* denotes training the classifier using the complete real training set \mathcal{R} , which serves as the theoretical upper bound of dataset distillation performance. Overall, the proposed DPD consistently outperforms all competing methods across all settings, demonstrating its effectiveness for remote sensing dataset distillation.

In particular, DPD shows clear advantages in low-data cases. When IPC is small (e.g., IPC = 5), DPD achieves significantly higher OA than existing methods, which indicates that the distilled samples generated by DPD are more informative and discriminative. Moreover, as IPC increases, the performance gap between DPD and baseline methods remains stable or even further widens. This suggests that the proposed method can effectively leverage additional synthetic samples for training without suffering from data redundancy.

It is also worth noting that DPD demonstrates strong generalization across different classification architectures. From lightweight models such as AlexNet and VGG16 to deeper networks including ResNet101, DenseNet201, and RegNetX-16GF, models trained on DPD-distilled datasets consistently achieve superior performance. This cross-architecture robustness further indicates that the distilled samples produced by DPD can capture intrinsic semantic characteristics of remote sensing scenes, rather than overfitting to a specific classifier.

We further report the computational cost of different dataset distillation methods in Table IV. The results summarize the GPU hours required for training the corresponding distillation models as well as for generating distilled samples with IPC = 20. We observe that diffusion-based distillation models built upon DiT-style architectures, such as DiT and Minimax Diffusion, generally exhibit lower training cost. In contrast, autoregressive text-to-image models such as Txt2Img-MHN tend

TABLE III
DATASET DISTILLATION PERFORMANCE IN TERMS OF OA (%) ON THE NWPU DATASET ACROSS DIFFERENT CLASSIFICATION NETWORKS.

IPC (Ratio)	Method	AlexNet	VGG16	Inception-v3	ResNet18	ResNet101	DenseNet121	DenseNet201	RegNetX-16GF
3 (0.5%)	Txt2Img-MHN [17]	23.88±1.22	19.59±0.65	13.82±0.75	17.71±2.30	23.82±1.68	16.42±1.29	22.04±1.30	24.32±1.86
	DiT [43]	20.75±1.68	14.48±1.94	15.72±1.31	19.79±1.04	24.56±1.58	17.73±1.08	23.27±0.87	25.52±1.31
	Minimax Diffusion [14]	15.86±1.11	11.92±2.77	11.85±0.77	15.03±1.58	18.76±1.08	13.38±1.38	17.37±1.03	19.88±1.40
	Stable Diffusion 2 [41]	27.51±2.33	30.17±4.13	32.56±1.50	35.53±1.42	41.81±2.14	36.86±1.26	42.72±1.33	44.88±2.99
5 (0.8%)	DPD (ours)	32.32±2.62	31.52±2.22	34.89±1.88	39.44±1.61	48.33±1.08	38.52±1.33	46.14±1.20	49.95±1.26
	Txt2Img-MHN [17]	29.17±0.84	19.17±2.86	16.71±1.04	21.66±0.91	26.43±2.10	20.80±1.39	27.01±1.71	25.28±0.96
	DiT [43]	26.83±1.24	14.95±2.35	19.23±1.71	23.52±1.70	27.22±1.85	22.80±1.69	25.56±1.78	28.32±1.73
	Minimax Diffusion [14]	18.10±1.58	10.07±2.27	14.42±0.78	16.30±0.99	17.04±2.45	14.92±1.25	15.94±1.13	19.94±1.57
10 (1.7%)	Stable Diffusion 2 [41]	29.63±2.52	28.83±5.44	39.83±1.64	39.74±2.17	44.17±3.86	42.58±1.58	46.30±2.16	44.71±3.33
	DPD (ours)	42.35±1.72	39.86±3.60	45.70±1.04	47.34±1.74	54.59±1.72	48.34±2.43	55.09±2.17	54.65±2.07
	Txt2Img-MHN [17]	37.40±2.14	29.73±2.38	25.88±2.86	30.35±1.27	33.24±0.68	31.19±1.30	36.13±1.07	30.92±2.15
	DiT [43]	32.61±1.62	24.68±3.30	27.55±1.34	31.59±1.23	32.60±2.92	31.33±0.77	35.02±1.75	37.62±2.08
15 (2.5%)	Minimax Diffusion [14]	24.05±1.41	15.95±3.84	19.80±1.26	24.59±1.32	22.60±2.24	22.25±1.66	26.90±1.63	26.78±3.06
	Stable Diffusion 2 [41]	37.14±2.67	34.93±3.08	47.48±1.27	41.56±2.47	42.94±3.34	48.94±1.65	50.86±2.48	44.78±3.38
	DPD (ours)	50.91±1.45	46.39±4.95	57.24±0.98	58.05±1.15	60.62±2.81	61.56±1.59	65.90±1.08	63.51±1.61
	Txt2Img-MHN [17]	40.08±2.06	33.38±2.47	31.17±1.31	35.31±0.95	36.28±1.31	36.05±1.54	39.18±1.68	36.90±3.99
20 (3.3%)	DiT [43]	40.20±1.30	28.64±4.19	38.86±0.96	38.56±1.63	44.21±2.28	41.45±1.70	45.84±2.22	46.64±1.65
	Minimax Diffusion [14]	28.66±2.44	24.51±3.46	25.98±1.57	29.45±1.52	29.06±3.07	29.84±1.50	34.57±1.72	34.74±1.21
	Stable Diffusion 2 [41]	35.42±1.71	36.70±3.06	48.61±1.42	44.57±2.60	45.45±2.20	50.89±3.11	54.41±2.25	49.02±3.30
	DPD (ours)	51.57±2.54	50.35±5.41	62.23±1.14	61.13±1.90	65.14±1.80	65.32±1.44	69.28±0.93	66.41±2.29
– (100%)	Full-data Training	87.49±0.75	89.76±0.83	93.64±0.39	92.64±0.51	92.88±0.70	94.92±0.52	95.06±0.47	94.72±0.46

Note: Best results are shown in **bold**. Here, Ratio = IPC \times $C/|\mathcal{R}|$ denotes the proportion of distilled samples to the total number of training samples, where C is the number of classes in the training set \mathcal{R} .



Fig. 4. Qualitative comparison of randomly selected real images and distilled images generated by different dataset distillation methods on the UCM, AID, and NWPU datasets (IPC = 5). Note that all results are shown without manual “cherry picking”.

to be more efficient during the sample generation stage. Due to the introduction of clustering-based guidance, the proposed DPD incurs additional cost during sample generation. Overall, DPD achieves a favorable balance between model training cost and sample generation efficiency.

E. Qualitative Results

Figure 4 presents a qualitative comparison between randomly selected real images and distilled images generated by different dataset distillation methods on the UCM, AID, and NWPU datasets with IPC = 5. As shown in the figure,

existing methods exhibit varying degrees of limitations in terms of visual realism and sample diversity. For instance, Stable Diffusion 2 tends to produce visually plausible samples but suffers from limited intra-class diversity, often resulting in highly similar layouts or repetitive structures. In contrast, methods such as Minimax Diffusion may generate more diverse samples, but often introduce noticeable artifacts or exhibit degraded visual fidelity.

By comparison, the proposed DPD consistently generates distilled samples that are both visually realistic and diverse across different scene categories and datasets. As illustrated in the airplane, viaduct, and stadium classes, DPD not only

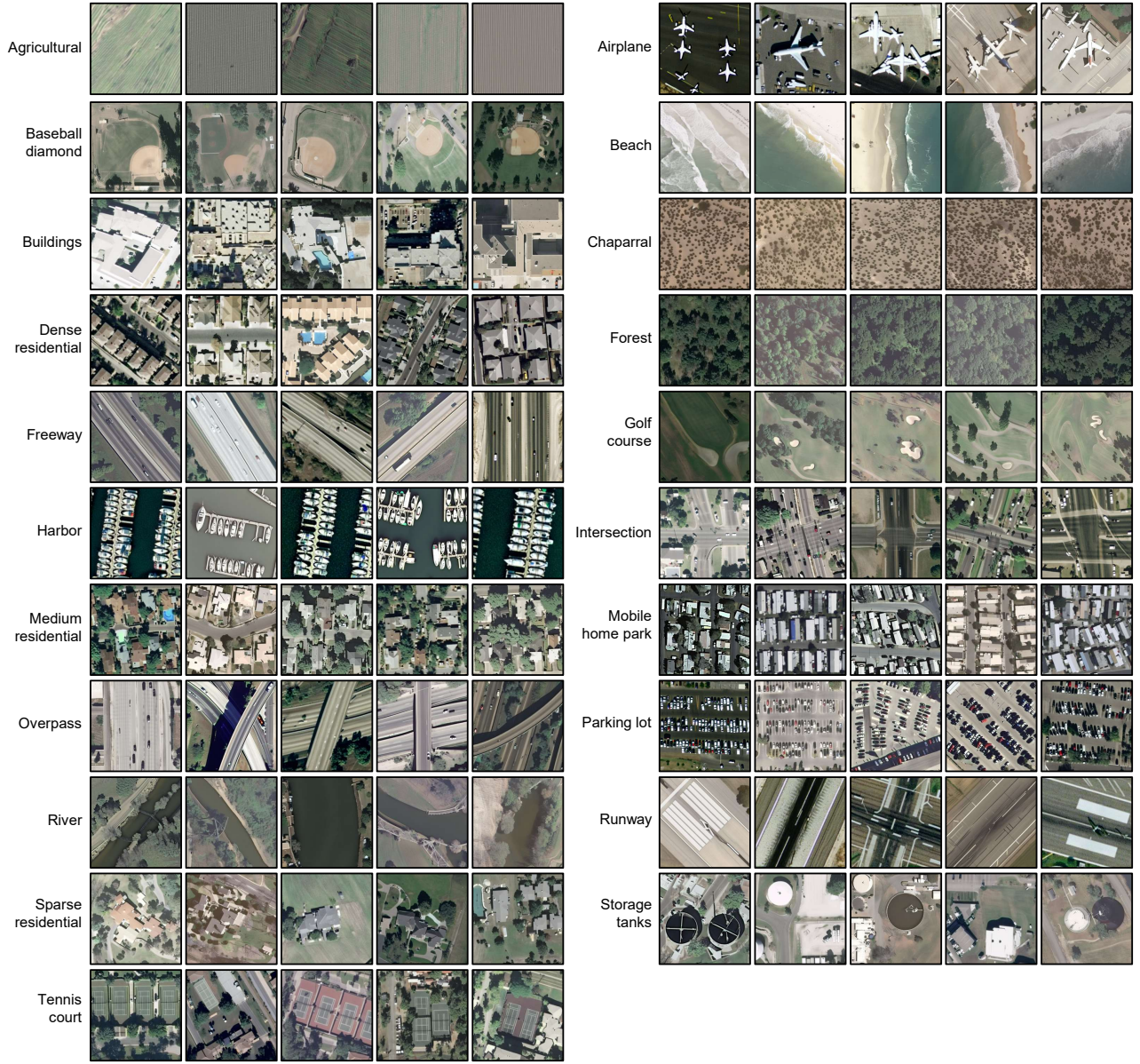


Fig. 5. Visualization of distilled images across 21 classes on the UCM dataset (IPC = 5). Note that all results are shown without manual “cherry picking”.

TABLE IV
COMPUTATIONAL COST OF DIFFERENT DATASET DISTILLATION METHODS.

Method	UCM		AID		NWPU	
	Train. (h)	Gen. (h)	Train. (h)	Gen. (h)	Train. (h)	Gen. (h)
Txt2Img-MHN	263.81	0.03	245.04	0.04	246.60	0.07
DiT	13.75	0.09	13.36	0.14	13.17	0.21
Minimax Diffusion	21.31	0.09	22.01	0.14	17.46	0.22
Stable Diffusion 2	106.80	0.28	85.92	0.43	75.21	0.62
DPD (ours)	136.56	0.35	115.15	0.56	104.62	1.05

Note: For each dataset, the lowest training or generation cost is highlighted in **bold**. Train. and Gen. denote the GPU hours required for training the distillation model and generating distilled samples with IPC = 20, respectively.

preserves key structural and semantic characteristics of real remote sensing images like object shapes and surrounding contexts, but also captures substantial variations in viewpoint, scale, and background environment. These qualitative observations indicate that the proposed DPD method can effectively

balances realism and diversity during the dataset distillation process, which is well aligned with the quantitative results reported in Section IV-D.

Figures 5–7 further provide comprehensive visualizations of the distilled images generated by the proposed method across all classes on the UCM, AID, and NWPU datasets. It is worth noting that all results are presented without any manual “cherry picking”.

F. Ablation Study and Parameter Analysis

To analyze the contribution of each component in the proposed DPD framework, we conduct an ablation study on the UCM, AID, and NWPU datasets with IPC = 10. As shown in Table V, the baseline model that only employs the diffusion loss \mathcal{L}_D yields relatively low performance across all three datasets. Introducing the classification consistency loss \mathcal{L}_{cls}

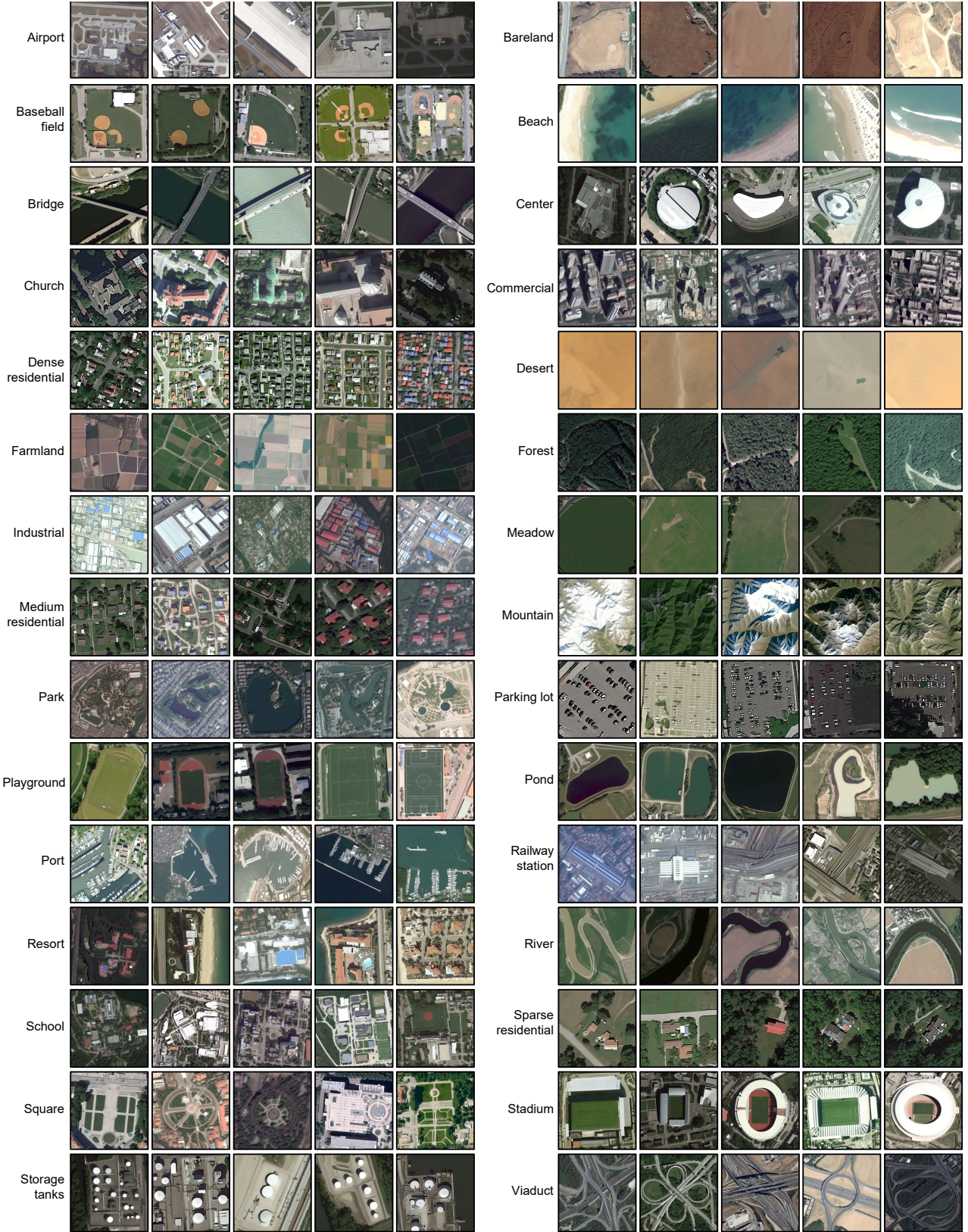


Fig. 6. Visualization of distilled images across 30 classes on the AID dataset (IPC = 5). Note that all results are shown without manual “cherry picking”.

leads to a substantial performance improvement by nearly 20 percentage points on UCM and AID, and over 25 percentage points on NWPU, which highlights the importance of

explicit discriminative supervision for enhancing the semantic relevance of distilled samples. Further incorporating visual prototype guidance brings additional significant performance

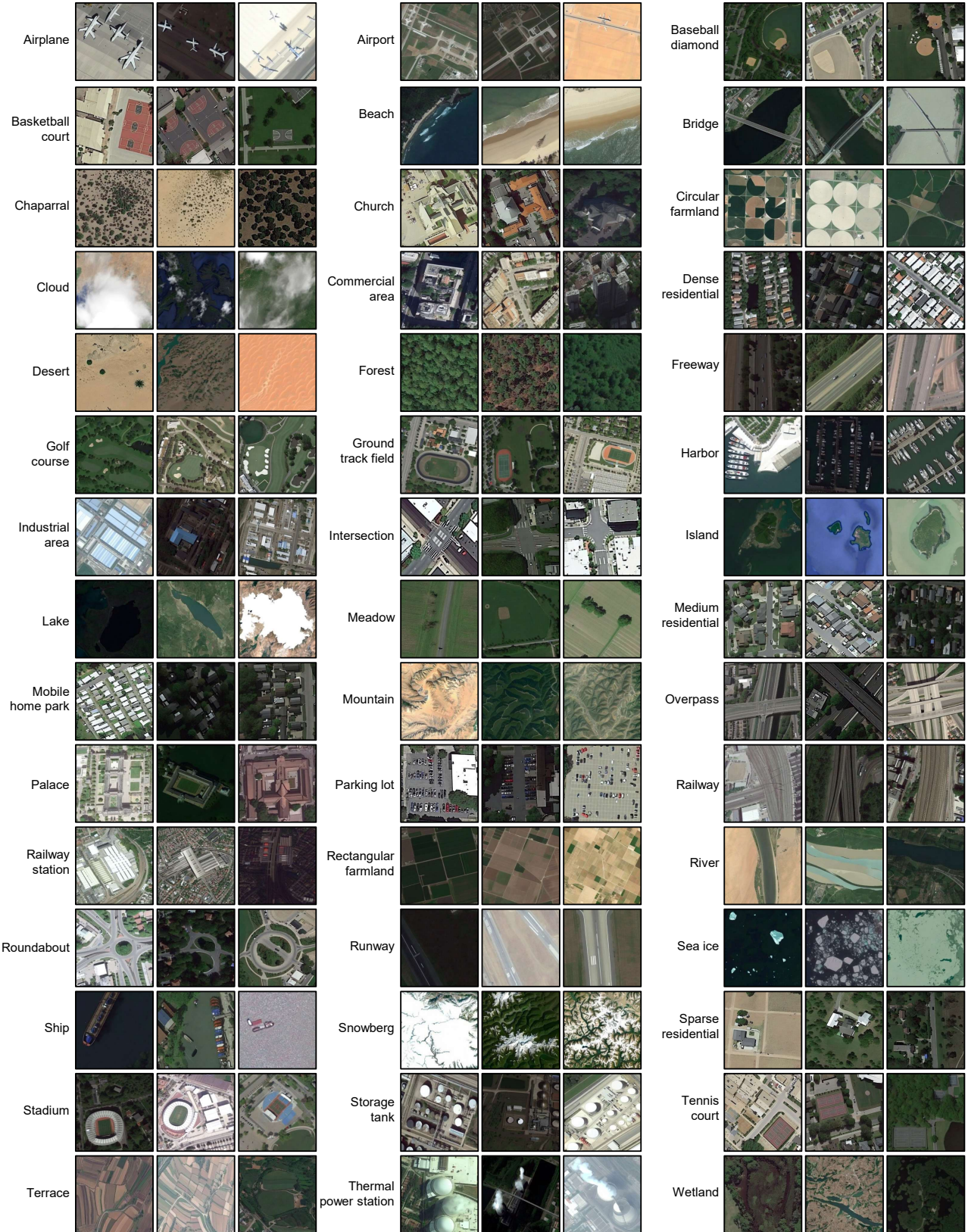


Fig. 7. Visualization of distilled images across 45 classes on the NWPU dataset (IPC = 3). Note that all results are shown without manual “cherry picking”.

gains, particularly on the UCM dataset, indicating that representative and diverse visual prototypes can effectively improve the structural diversity and semantic coverage of the generated

samples.

We further observe that caption aggregation exhibits different effects across datasets. On the UCM dataset, the best

TABLE V

ABLATION STUDY OF THE PROPOSED DPD ON THE UCM, AID, AND NWPU DATASETS WITH IPC = 10.

\mathcal{L}_D	\mathcal{L}_{cls}	Vis. Prot.	Cap. Agg.	UCM	AID	NWPU
✓				31.89 \pm 1.46	33.25 \pm 1.51	20.97 \pm 1.33
✓	✓			50.31 \pm 1.79	52.35 \pm 1.03	47.62 \pm 2.07
✓	✓	✓		79.38\pm0.83	67.33 \pm 1.27	57.09 \pm 1.62
✓	✓	✓	✓	78.30 \pm 0.98	70.86\pm1.45	58.05\pm1.15

Note: Best results are shown in **bold**. Performance is reported in OA (%) using ResNet18 as the classification network. Vis. Prot. and Cap. Agg. denote Visual Prototype and Caption Aggregation, respectively.

performance is achieved without caption aggregation, whereas AID and NWPU consistently benefit from its inclusion. This phenomenon can be attributed to variations in scene complexity and intra-class diversity among different datasets. UCM mainly consists of relatively simple and well-aligned scenes, where visual prototypes alone are sufficient to capture the dominant class semantics. In contrast, AID and NWPU exhibit higher intra-class variability in terms of scale and scene composition. In such cases, aggregating multiple captions can further enrich the semantic conditioning space, leading to more diverse and discriminative synthetic samples.

In addition to the ablation study, we further analyze the sensitivity of the proposed DPD framework to two key hyperparameters, including the classification consistency weight λ in Eq. (5) and the number of diffusion steps T used during the distillation stage. Figure 8(a) illustrates the effect of varying λ on the distillation performance across three datasets. When $\lambda = 0$, the model is trained using only the diffusion objective, and the generation process is guided by the extracted vision-language prototypes, which leads to relatively lower performance. Introducing a moderate classification consistency constraint consistently improves performance on all datasets, indicating that explicit discriminative supervision effectively guides the generation of semantically aligned distilled samples. However, excessively large values of λ tend to slightly degrade performance. Overall, $\lambda = 0.3$ achieves a favorable balance across all three datasets, and we adopt $\lambda = 0.3$ in all experiments.

Figure 8(b) shows the impact of the number of diffusion steps T during the distillation process. Increasing T from a small value generally leads to improved performance, as a larger number of diffusion steps allow the generative process to better refine structural details and semantic consistency. Nevertheless, the performance gains gradually saturate as T increases, and even exhibit a slight decline on some datasets when T becomes excessively large. Considering both performance and computational efficiency, we set $T = 50$ as a practical trade-off in all experiments.

V. CONCLUSION

In this paper, we present the first systematic study of dataset distillation for remote sensing image classification and demonstrate that large-scale remote sensing datasets can be effectively condensed into compact, fully synthetic alternatives without exposing any original data. Specifically, we propose a discriminative prototype-guided diffusion (DPD) framework

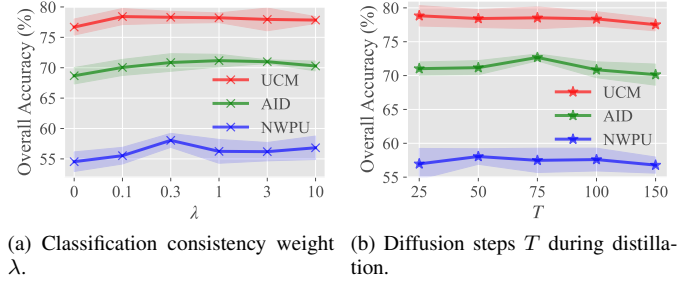


Fig. 8. Parameter analysis of the proposed method on the UCM, AID, and NWPU datasets with IPC = 10 using ResNet18.

that incorporates classifier-driven guidance into the diffusion training process to generate semantically discriminative and visually realistic distilled samples. Furthermore, we introduce a dual-guidance strategy that jointly leverages representative visual prototypes and cluster-level textual descriptions to enhance both the diversity and semantic richness of the synthesized data. Extensive experiments on three high-resolution remote sensing scene classification benchmarks validate the effectiveness of the proposed method in supporting downstream model training.

Since this work mainly focuses on dataset distillation for image-level scene classification, extending existing distillation frameworks to more fine-grained remote sensing interpretation tasks, such as land use and land cover classification, still remains an open challenge. We will explore it in our future research.

REFERENCES

- [1] X. X. Zhu, D. Tuia, L. Mou, G.-S. Xia, L. Zhang, F. Xu, and F. Fraundorfer, “Deep learning in remote sensing: A comprehensive review and list of resources,” *IEEE Geosci. Remote Sens. Mag.*, vol. 5, no. 4, pp. 8–36, 2017.
- [2] Q. Weng, Z. Li, Y. Cao, X. Lu, P. Gamba, X. Zhu, Y. Xu, F. Zhang, R. Qin, M. Y. Yang *et al.*, “How will ai transform urban observing, sensing, imaging, and mapping?” *npj Urban Sustainability*, vol. 4, no. 1, p. 50, 2024.
- [3] A. Ma, Y. Wan, Y. Zhong, J. Wang, and L. Zhang, “Scenenet: Remote sensing scene classification deep learning network using multi-objective neural evolution architecture search,” *ISPRS J. Photogramm. Remote Sens.*, vol. 172, pp. 171–188, 2021.
- [4] G.-S. Xia, X. Bai, J. Ding, Z. Zhu, S. Belongie, J. Luo, M. Datcu, M. Pelillo, and L. Zhang, “Dota: A large-scale dataset for object detection in aerial images,” in *Proc. IEEE Conf. Comput. Vis. Pattern Recognit.*, 2018, pp. 3974–3983.
- [5] L. Wang, R. Li, C. Zhang, S. Fang, C. Duan, X. Meng, and P. M. Atkinson, “Unetformer: A unet-like transformer for efficient semantic segmentation of remote sensing urban scene imagery,” *ISPRS J. Photogramm. Remote Sens.*, vol. 190, pp. 196–214, 2022.
- [6] L. Zhang and L. Zhang, “Artificial intelligence for remote sensing data analysis: A review of challenges and opportunities,” *IEEE Geosci. Remote Sens. Mag.*, vol. 10, no. 2, pp. 270–294, 2022.
- [7] M. Schmitt, S. A. Ahmadi, Y. Xu, G. Taşkin, U. Verma, F. Sica, and R. Hänsch, “There are no data like more data: Datasets for deep learning in earth observation,” *IEEE Geosci. Remote Sens. Mag.*, vol. 11, no. 3, pp. 63–97, 2023.
- [8] X. Sun, B. Wang, Z. Wang, H. Li, H. Li, and K. Fu, “Research progress on few-shot learning for remote sensing image interpretation,” *IEEE J. Sel. Topics Appl. Earth Observ. Remote Sens.*, vol. 14, pp. 2387–2402, 2021.
- [9] Y. Xu, T. Bai, W. Yu, S. Chang, P. M. Atkinson, and P. Ghamisi, “Ai security for geoscience and remote sensing: Challenges and future trends,” *IEEE Geosci. Remote Sens. Mag.*, vol. 11, no. 2, pp. 60–85, 2023.

[10] P. Ghamisi, W. Yu, A. Marinoni, C. M. Gevaert, C. Persello, S. Selvakumaran, M. Girotto, B. P. Horton, P. Rufin, P. Hostert, F. Pacifici, and P. M. Atkinson, "Responsible artificial intelligence for earth observation: Achievable and realistic paths to serve the collective good," *IEEE Geosci. Remote Sens. Mag.*, 2025.

[11] S. Lei and D. Tao, "A comprehensive survey of dataset distillation," *IEEE Trans. Pattern Anal. Mach. Intell.*, vol. 46, no. 1, pp. 17–32, 2023.

[12] R. Yu, S. Liu, and X. Wang, "Dataset distillation: A comprehensive review," *IEEE Trans. Pattern Anal. Mach. Intell.*, vol. 46, no. 1, pp. 150–170, 2023.

[13] T. Wang, J.-Y. Zhu, A. Torralba, and A. A. Efros, "Dataset distillation," *arXiv preprint arXiv:1811.10959*, 2018.

[14] J. Gu, S. Vahidian, V. Kungurtsev, H. Wang, W. Jiang, Y. You, and Y. Chen, "Efficient dataset distillation via minimax diffusion," in *Proc. IEEE Conf. Comput. Vis. Pattern Recognit.*, 2024, pp. 15 793–15 803.

[15] L. Zhao, Y. Wu, X. Jiang, J. Gu, Y. Wang, X. Xu, P. Zhao, and X. Lin, "Taming diffusion for dataset distillation with high representativeness," in *Proc. Int. Conf. Mach. Learn.*, 2025.

[16] L. Zhang, L. Zhang, and B. Du, "Deep learning for remote sensing data: A technical tutorial on the state of the art," *IEEE Geosci. Remote Sens. Mag.*, vol. 4, no. 2, pp. 22–40, 2016.

[17] Y. Xu, W. Yu, P. Ghamisi, M. Kopp, and S. Hochreiter, "Txt2img-mhn: Remote sensing image generation from text using modern hopfield networks," *IEEE Trans. Image Process.*, vol. 32, pp. 5737–5750, 2023.

[18] R. Zhao and Z. Shi, "Text-to-remote-sensing-image generation with structured generative adversarial networks," *IEEE Geosci. Remote Sens. Lett.*, vol. 19, pp. 1–5, 2021.

[19] D. Tang, X. Cao, X. Hou, Z. Jiang, J. Liu, and D. Meng, "Crs-diff: Controllable remote sensing image generation with diffusion model," *IEEE Trans. Geos. Remote Sens.*, 2024.

[20] T. Salimans, I. Goodfellow, W. Zaremba, V. Cheung, A. Radford, and X. Chen, "Improved techniques for training GANs," in *Proc. Neural Inf. Process. Syst.*, vol. 29, 2016.

[21] M. Heusel, H. Ramsauer, T. Unterthiner, B. Nessler, and S. Hochreiter, "Gans trained by a two time-scale update rule converge to a local nash equilibrium," in *Proc. Neural Inf. Process. Syst.*, vol. 30, 2017.

[22] E. Strubell, A. Ganesh, and A. McCallum, "Energy and policy considerations for modern deep learning research," in *Proc. AAAI Conf. Artif. Intell.*, vol. 34, no. 09, 2020, pp. 13 693–13 696.

[23] O. Bohdal, Y. Yang, and T. M. Hospedales, "Flexible dataset distillation: Learn labels instead of images," in *Workshop on Meta-Learning at NeurIPS*, 2020.

[24] I. Sucholutsky and M. Schonlau, "Soft-label dataset distillation and text dataset distillation," in *Proc. Int. Joint Conf. Neural Netw. IEEE*, 2021, pp. 1–8.

[25] B. Zhao, K. R. Mopuri, and H. Bilen, "Dataset condensation with gradient matching," in *Proc. Int. Conf. Learn. Representations*, 2021.

[26] G. Cazenavette, T. Wang, A. Torralba, A. A. Efros, and J.-Y. Zhu, "Dataset distillation by matching training trajectories," in *Proc. IEEE Conf. Comput. Vis. Pattern Recognit.*, 2022, pp. 4750–4759.

[27] B. Zhao and H. Bilen, "Dataset condensation with distribution matching," in *Proc. IEEE Winter Conf. Appl. Comput. Vis.*, 2023, pp. 6514–6523.

[28] K. Wang, J. Gu, J. Gu, H. Zhang, D. Zhou, Z. Zhu, W. Jiang, and Y. You, "Dim: Distilling dataset into generative model," in *Proc. Eur. Conf. Comput. Vis.* Springer, 2024, pp. 42–59.

[29] D. Su, J. Hou, W. Gao, Y. Tian, and B. Tang, "D⁴: Dataset distillation via disentangled diffusion model," in *Proc. IEEE Conf. Comput. Vis. Pattern Recognit.*, 2024, pp. 5809–5818.

[30] A. Ramesh, M. Pavlov, G. Goh, S. Gray, C. Voss, A. Radford, M. Chen, and I. Sutskever, "Zero-shot text-to-image generation," in *Proc. Int. Conf. Mach. Learn.*, 2021, pp. 8821–8831.

[31] X. Li, C. Wen, Y. Hu, Z. Yuan, and X. X. Zhu, "Vision-language models in remote sensing: Current progress and future trends," *IEEE Geosci. Remote Sens. Mag.*, vol. 12, no. 2, pp. 32–66, 2024.

[32] Y. Liu, J. Yue, S. Xia, P. Ghamisi, W. Xie, and L. Fang, "Diffusion models meet remote sensing: Principles, methods, and perspectives," *IEEE Trans. Geos. Remote Sens.*, 2024.

[33] S. Khanna, P. Liu, L. Zhou, C. Meng, R. Rombach, M. Burke, D. B. Lobell, and S. Ermon, "Diffusionsat: A generative foundation model for satellite imagery," in *Proc. Int. Conf. Learn. Representations*.

[34] Z. Zhang, T. Zhao, Y. Guo, and J. Yin, "Rs5m and georsclip: A large scale vision-language dataset and a large vision-language model for remote sensing," *IEEE Trans. Geos. Remote Sens.*, 2024.

[35] C. Liu, K. Chen, R. Zhao, Z. Zou, and Z. Shi, "Text2earth: Unlocking text-driven remote sensing image generation with a global-scale dataset and a foundation model," *IEEE Geosci. Remote Sens. Mag.*, 2025.

[36] B. Büyüktas, G. Sumbul, and B. Demir, "Federated learning across decentralized and unshared archives for remote sensing image classification: A review," *IEEE Geosci. Remote Sens. Mag.*, vol. 12, no. 3, pp. 64–80, 2024.

[37] X. Zhang, B. Zhang, W. Yu, and X. Kang, "Federated deep learning with prototype matching for object extraction from very-high-resolution remote sensing images," *IEEE Trans. Geos. Remote Sens.*, vol. 61, pp. 1–16, 2023.

[38] H. Lin, C. Zhang, D. Hong, K. Dong, and C. Wen, "Fedrsclip: Federated learning for remote sensing scene classification using vision-language models," *IEEE Geosci. Remote Sens. Mag.*, 2025.

[39] Z. Zhang, X. Ma, and J. Ma, "Local differential privacy based membership-privacy-preserving federated learning for deep-learning-driven remote sensing," *Remote Sensing*, vol. 15, no. 20, p. 5050, 2023.

[40] J. Ho, A. Jain, and P. Abbeel, "Denoising diffusion probabilistic models," in *Advances in Neural Information Processing Systems*, 2020, pp. 6840–6851.

[41] R. Rombach, A. Blattmann, D. Lorenz, P. Esser, and B. Ommer, "High-resolution image synthesis with latent diffusion models," in *Proc. IEEE Conf. Comput. Vis. Pattern Recognit.*, 2022, pp. 10 684–10 695.

[42] A. Radford, J. W. Kim, C. Hallacy, A. Ramesh, G. Goh, S. Agarwal, G. Sastry, A. Askell, P. Mishkin, J. Clark *et al.*, "Learning transferable visual models from natural language supervision," in *Proc. Int. Conf. Mach. Learn.* PMLR, 2021, pp. 8748–8763.

[43] W. Peebles and S. Xie, "Scalable diffusion models with transformers," in *Proc. IEEE Int. Conf. Comput. Vis.*, 2023, pp. 4195–4205.

[44] Y. Yang and S. Newsam, "Bag-of-visual-words and spatial extensions for land-use classification," in *Proc. SIGSPATIAL Int. Conf. Adv. Geographic Inf. Syst.* ACM, 2010, pp. 270–279.

[45] G.-S. Xia, J. Hu, F. Hu, B. Shi, X. Bai, Y. Zhong, L. Zhang, and X. Lu, "Aid: A benchmark data set for performance evaluation of aerial scene classification," *IEEE Trans. Geosci. Remote Sens.*, vol. 55, no. 7, pp. 3965–3981, 2017.

[46] G. Cheng, J. Han, and X. Lu, "Remote sensing image scene classification: Benchmark and state of the art," *Proc. IEEE*, vol. 105, no. 10, pp. 1865–1883, 2017.

[47] A. Krizhevsky, I. Sutskever, and G. E. Hinton, "Imagenet classification with deep convolutional neural networks," *Proc. Neural Inf. Process. Syst.*, vol. 25, pp. 1097–1105, 2012.

[48] K. Simonyan and A. Zisserman, "Very deep convolutional networks for large-scale image recognition," *arXiv preprint arXiv:1409.1556*, 2014.

[49] C. Szegedy, V. Vanhoucke, S. Ioffe, J. Shlens, and Z. Wojna, "Rethinking the inception architecture for computer vision," in *Proc. IEEE Conf. Comput. Vis. Pattern Recognit.*, 2016, pp. 2818–2826.

[50] K. He, X. Zhang, S. Ren, and J. Sun, "Deep residual learning for image recognition," in *Proc. IEEE Conf. Comput. Vis. Pattern Recognit.*, 2016, pp. 770–778.

[51] G. Huang, Z. Liu, L. Van Der Maaten, and K. Q. Weinberger, "Densely connected convolutional networks," in *Proc. IEEE Conf. Comput. Vis. Pattern Recognit.*, 2017, pp. 4700–4708.

[52] I. Radosavovic, R. P. Kosaraju, R. Girshick, K. He, and P. Dollár, "Designing network design spaces," in *Proc. IEEE Conf. Comput. Vis. Pattern Recognit.*, 2020, pp. 10 428–10 436.

[53] G. Ilharco, M. Wortsman, R. Wightman, C. Gordon, N. Carlini, R. Taori, A. Dave, V. Shankar, H. Namkoong, J. Miller, H. Hajishirzi, A. Farhadi, and L. Schmidt, "Openclip," Jul. 2021.

[54] C. Schuhmann, R. Beaumont, R. Vencu, C. W. Gordon, R. Wightman, M. Cherti, T. Coombes, A. Katta, C. Mullis, M. Wortsman, P. Schramowski, S. R. Kundurthy, K. Crowson, L. Schmidt, R. Kaczmarczyk, and J. Jitsev, "LAION-5b: An open large-scale dataset for training next generation image-text models," in *Proc. Neural Inf. Process. Syst.*, 2022.

[55] S. Bai, K. Chen, X. Liu, J. Wang, W. Ge, S. Song, K. Dang, P. Wang, S. Wang, J. Tang *et al.*, "Qwen2.5-v1 technical report," *arXiv preprint arXiv:2502.13923*, 2025.

[56] E. J. Hu, Y. Shen, P. Wallis, Z. Allen-Zhu, Y. Li, S. Wang, L. Wang, W. Chen *et al.*, "Lora: Low-rank adaptation of large language models," in *Proc. Int. Conf. Learn. Representations*, 2022.

[57] I. Loshchilov and F. Hutter, "Decoupled weight decay regularization," *arXiv preprint arXiv:1711.05101*, 2017.

[58] K. D. B. J. Adam *et al.*, "A method for stochastic optimization," *arXiv preprint arXiv:1412.6980*, vol. 1412, no. 6, 2014.

[59] A. Yang, A. Li, B. Yang, B. Zhang, B. Hui, B. Zheng, B. Yu, C. Gao, C. Huang, C. Lv *et al.*, "Qwen3 technical report," *arXiv preprint arXiv:2505.09388*, 2025.